

# UC Santa Barbara

## UC Santa Barbara Previously Published Works

### Title

Subaqueous clinoforms created by sandy wave-supported gravity flows: Lessons from the Central California shelf

### Permalink

<https://escholarship.org/uc/item/62t4p940>

### Authors

Medri, Elisa  
Simms, Alexander R  
Kluesner, Jared  
[et al.](#)

### Publication Date

2023-02-01

### DOI

10.1016/j.margeo.2022.106977

Peer reviewed

1  
2  
3  
4  
5  
6  
7  
8  
9  
10  
11  
12  
13  
14  
15  
16  
17  
18  
19  
20  
21  
22  
23  
24  
25  
26  
27  
28  
29  
30  
31  
32  
33  
34

## **Subaqueous clinoforms created by sandy wave-supported gravity flows: lessons from the central California shelf**

Elisa Medri<sup>1</sup>, Alexander R. Simms<sup>1</sup>, Jared Kluesner<sup>2</sup>, Samuel Y. Johnson<sup>2</sup>, Stuart P. Nishenko<sup>3</sup>, H. Gary Greene<sup>4</sup> and James E. Conrad<sup>2</sup>

<sup>1</sup> University of California, Santa Barbara, Santa Barbara, CA, USA

<sup>2</sup> U.S. Geological Survey, Santa Cruz, CA, USA

<sup>3</sup> Pacific Gas and Electric, San Francisco, CA, USA

<sup>4</sup> Moss Landing Marine Laboratories, CA, USA

Corresponding Author:

Elisa Medri

emedri@ucsb.edu

### **Abstract**

Subaqueous clinoforms are an important shelf feature. Their origins are typically associated with subaerial deltas but recent work has identified similar features in settings without a significant fluvial source (Mitchell, 2012; Patruno et al., 2015; Patruno and Helland-Hansen, 2018). These other studies have shown that such subaqueous clinoforms, also known as infralittoral prograding wedges (IPWs), are created largely by wave-induced processes. This study uses geophysical, sedimentological, and radiocarbon data to determine the sedimentary characteristics and genesis of a shore-parallel subaqueous clinoform developed far from any significant river on the central California continental shelf; a sedimentary shelf buildup known locally as the Cross Hosgri Slope. Sediment cores through the clinoformal sedimentary unit reveal that it is composed of beds with an erosive base, overlain by a thin (~15 cm) coarsening upward sequence of shelly fine sands transitioning to a fining upward sequence marked by alternating parallel and ripple cross laminated very fine sands. The sedimentary succession is often capped by fine silts that are commonly interbedded with thin very fine sand beds. Radiocarbon dating of shells collected just above the erosive base indicate the subaqueous clinoform initiated progradation ~7 ka, nucleating on an older Younger Dryas relict shoreface. We suggest the Cross Hosgri Slope was created by winter-storm waves mobilizing sands in water depths up to ~70 m that transitioned into wave-

35 supported gravity flows. The wave-supported gravity flows traveled downslope to water  
36 depths of up to ~80 m, corresponding to the foot of the subaqueous clinoform. They did not  
37 travel beyond this depth as wave influence at these depths is negligible and the shelf gradient  
38 is insufficient to maintain movement of the load alone. Our work suggests that wave-  
39 supported gravity flows can entrain very fine sands and silts and build subaqueous  
40 clinoforms, even in the absence of a significant river source. Furthermore, we provide a  
41 facies model for sandy wave-supported gravity flow deposits.

42  
43 *Keywords:* Shelf processes; Gravity flows; Pacific Ocean; Sedimentary facies; Holocene;  
44 Quaternary stratigraphy

45  
46

## 47 **1. Introduction**

48 Subaqueous clinoforms are inclined, basin-dipping strata, generally sigmoidal in shape,  
49 with a typical rollover point at water depths up to 60 m (Cattaneo and Steel, 2003; Mitchell,  
50 2012; Patruno et al., 2015; Patruno and Helland-Hansen, 2018; Steel and Olsen, 2002).  
51 Subaqueous clinoforms are commonly observed as part of a compound system (Patruno et al.,  
52 2015; Patruno and Helland-Hansen, 2018) associated with fluvial-deltaic systems.

53 Subaqueous clinoforms can also occur in isolation, not connected to fluvial-deltaic  
54 systems (Budillon et al., 2022; Fernández-Salas et al., 2009; Hernandez-Molina et al., 2000;  
55 Martínez-Carreño et al., 2017). In these cases, the processes responsible for advection of  
56 sediment can be different, and mainly dominated by basin dynamics, such as waves, currents,  
57 and tides, rather than direct fluvial input (Patruno et al., 2015; Pirmez et al., 1998).  
58 Contouritic clinoforms form in areas with little fluvial input, and are mainly driven by bottom  
59 currents (Schattner et al., 2020). However, contouritic clinoforms usually occur along the  
60 shelf edge and the upper slope, at greater water depths than the ones discussed in this study.  
61 Another feeding mechanism are wave-supported gravity flows (WSGFs), capable of moving

62 large amounts of sediment across continental shelves (Ozdemir, 2016; Traykovski et al.,  
63 2007). WSGFs are the result of resuspension of sediment by wave energy, generating a high-  
64 density layer near the seabed that moves downslope, and eventually dissipates when wave  
65 energy is not sufficient to maintain sediment entrainment (Flores et al., 2018; Ma et al.,  
66 2008). On energetic continental shelves, wave influence can create high-density turbulence  
67 layers and enough shear stress to remobilize sediments in shallow coastal areas and promote  
68 their downslope movement to distal areas of continental shelves (Flores et al., 2018;  
69 Ozdemir, 2016; Traykovski et al., 2007; Wright et al., 2001; Wright and Friedrichs, 2006).  
70 The literature investigating WSGFs is relatively small, and these processes have mainly been  
71 recorded in association with large river floods, mobilizing exclusively mud-sized grains (Ma  
72 et al., 2008; Ogston et al., 2000; Scully et al., 2003). While this has been observed on river-  
73 derived, fine-grained sediments, Flores et al. (2018) showed that the same conditions can be  
74 attained in sandy environments without an associated river flood, indicating that this  
75 phenomenon may occur in a wider range of settings than previously reported. Furthermore,  
76 while a growing number of papers focus on modeling WSGF processes and dynamics  
77 (Ozdemir, 2016; Puig et al., 2003; Scully et al., 2003; Traykovski et al., 2007; Wright et al.,  
78 2001; Wright and Friedrichs, 2006), observation of their deposits and associated facies –  
79 specifically sandy WSGFs – are rare.

80 The continental shelf of central California is characterized by a high-energy wave climate  
81 (Storlazzi and Wingfield, 2005) and is marked by numerous sandy, coast-parallel to  
82 subparallel geomorphic features. One of these is informally known as the Cross Hosgri Slope  
83 (CHS), a southwest-facing sandy clinoform located at a water depth of ~70 m and ~2 km  
84 from the modern shoreline (Johnson et al., 2014; Fig. 1). Previously collected seismic-  
85 reflection data show that it is a subaqueous clinoform (Johnson et al., 2014). The purpose of  
86 this study is to describe and interpret the origin of the CHS and its deposits by analyzing

87 cores, high-resolution seismic chirp data, and <sup>14</sup>C ages. This study also provides a facies  
88 model for WSGF deposits in sandy environments, and could aid in the differentiation of their  
89 deposits from other offshore sand bodies such as overstepped barriers, drowned shorefaces,  
90 and other forms of sediment gravity flows.

## 91 **2. Regional setting**

### 92 *2.1 Waves, climate and watersheds*

93 The study area lies northwest of Estero Point, central California (Fig. 1). The region has a  
94 narrow (< 5 km) continental shelf offshore of the coastal Santa Lucia Mountains, which are  
95 incised by small, narrow ephemeral and perennial streams. The largest nearby stream is the  
96 ephemeral 123 km<sup>2</sup> Santa Rosa Creek watershed, which lies ~10 km north of the CHS. Santa  
97 Rosa Creek and the other nearby smaller streams flow unobstructed down steep hills mantled  
98 with shallow soils and sparse vegetation (Hawley et al., 2012).

99 The central California coast has a Mediterranean climate, with warm dry summers and  
100 cool, wet winters (Bakker and Slack, 1985). The climate is controlled by the North Pacific  
101 High, a high-pressure system resting over cold upwelling waters, which deflects storms from  
102 reaching the California coast during the summer months (Kämpf and Chapman, 2016).  
103 During winter, the Pacific High migrates to the south resulting in relatively high rainfall in  
104 California between November and March. Overall, the California coast experiences highly  
105 variable annual rainfall depending on storm frequency and magnitude. Mean annual rainfall  
106 in the Santa Lucia Range varies between 40 and 150 cm (Ramirez et al., 2020).

107 The central California coast is located in an area characterized by a high energy wave  
108 climate (Dingler et al., 1982), where average wave periods recorded at the closest wave buoy  
109 northwest of Estero Point can reach 10 s, with mean significant wave heights up to 5-6 m in  
110 the winter seasons (NOAA.gov; Storlazzi and Wingfield, 2005). The wave climate in central  
111 California is controlled by three main trends: (i) the north Pacific swell generated by cyclones

112 in the northern Pacific Ocean during winter months, (ii) a southern swell, generated by winter  
113 storms in the southern hemisphere during the northern hemisphere summer, and (iii) locally  
114 wind-driven waves (Storlazzi and Griggs, 2000; Storlazzi and Wingfield, 2005). Storm events  
115 in this region are greater during the winter months, specifically in the months of December  
116 and January. The north Pacific swell approaches from the west/northwest and is largest in  
117 October through May, producing the largest waves to impact this region (2–10 m height)  
118 (Storlazzi and Wingfield, 2005). The southern swell is more active in summer months, and  
119 approaches the coast from the west/southwest with wave heights between 0.3-3 m.

120         The main ocean current influencing the central California coast is the California  
121 Current; a wide, strong offshore current that flows south at a distance of ~100 – 200 km from  
122 the modern shoreline (Bray et al., 1999; Chelton, 1984; Collins et al., 2003; Hickey, 1998).  
123 The California Current reaches its strongest speeds of ~0.05 m/s at the surface and extends to  
124 ~ 500 m depth (Auad et al., 2011; Hickey, 1998). A narrower and weaker northward-flowing  
125 surface current develops north of Point Conception (Fig. 1b) at ~15-20 km offshore (Collins  
126 et al., 2003), reaching its maximum velocity during the winter months (Auad et al., 2011;  
127 Checkley and Barth, 2009; Chelton, 1984; Collins et al., 2003; Hickey, 1998; Reid and  
128 Schwartzlose, 1962).

129         Due to California’s location on the forebulge of the former Last Glacial Maximum ice  
130 sheets (Clark et al., 1978), relative sea level (RSL) at this location has risen continuously  
131 since the Last Glacial Maximum (Yousefi et al., 2018). However, the physical constraints on  
132 RSL history for the southern California coast are largely limited to the past 10-12 ka (Fig. 2)  
133 (Reynolds and Simms, 2015). Over this time period, relative sea level has risen  
134 approximately 60 m (Fig. 2).

## 135         2.2 Structural setting

136 The continental shelf off Estero Point, is a tectonically active region crossed by a series of  
137 north-south trending strike-slip faults, the largest of which is the Hosgri fault (Hanson et al.,  
138 1995; Johnson et al., 2018, 2014; Johnson and Watt, 2012; Langenheim et al., 2013;  
139 Nishenko et al., 2018). The Hosgri fault is part of the distributed right-lateral transform  
140 boundary between the Pacific Plate and the Sierran microplate, which include the larger San  
141 Andreas Fault to the east of the study area. Johnson et al. (2014) estimated a modern slip rate  
142 of  $2.6 \pm 0.9$  mm/yr for the Hosgri fault based on offset of the base of the CHS. Over the last  
143 11 Ma, the Hosgri fault is inferred to have experienced  $156 \pm 4$  km of slip (Dickinson et al.,  
144 2005).

### 145 *2.3 The Cross Hosgri Slope*

146 The Cross Hosgri Slope (CHS) is a shore-parallel sand body located 5 km northwest of  
147 Estero Point in water depths of  $\sim 70$  m (Fig. 1). Johnson et al. (2014) first described it as a  
148 southeast-striking feature, with a height of 7-9 m, a length of 1700 m, and a width of 250-280  
149 m. The feature is characterized by a slope of  $1.6^\circ - 2.0^\circ$  dipping to the SW, a considerably  
150 steeper angle than the surrounding seafloor to the northeast and southwest, which dips more  
151 gently at  $0.4^\circ - 0.6^\circ$  (Johnson et al., 2014). In the absence of sediment cores and radiocarbon  
152 ages, Johnson et al. (2014) interpreted the CHS to be a drowned shoreface paired to a now-  
153 eroded sandspit, and inferred a Younger Dryas age ( $\sim 12,800$  to  $11,500$  yr B.P.) based on the  
154 global sea-level curve of Stanford et al. (2011).

## 155 **3. Material and Methods**

### 156 *3.1 Chirp seismic-reflection survey*

157 From October 18<sup>th</sup>-24<sup>th</sup>, 2019, the U.S Geological Survey (USGS) Pacific Coastal and  
158 Marine Science Center (PCMSC), in collaboration with Pacific Gas and Electric (PG&E),  
159 obtained a total of 450 km of high-resolution chirp data from the central California shelf  
160 (Snyder et al., 2022). Six kilometers of these data are used in this study to examine the CHS.

161 These consist of 2 chirp lines, one crossing perpendicular to the CHS (HFC-05), and one  
162 parallel to the CHS (HFC-25). The high-resolution seismic survey was conducted aboard the  
163 M/V *Bold Horizon* using an Edgetech 2300-516 chirp sub bottom profiler. Chirp data were  
164 imported in Shearwater Reveal software and processed using the real (non-Hilbert  
165 transformed) traces and included navigation conversion, fish depth correction, multi-step well  
166 correction, predictive deconvolution, water column mute, and gain adjustment. The water  
167 depths of the survey varied between 30 and 200 m.

### 168 *3.2 Sediment cores*

169 Seven vibracores ranging in length from ~0.5 - 3.0 m were also collected from the CHS  
170 from the M/V *Bold Horizon* using a Rossfelder P-5 vibracore system. A transect of 3 core  
171 sites was collected perpendicular across the CHS and in line with one of the chirp profiles  
172 (Table 1; Fig. 1). Each of these sites was sampled with a pair of duplicate cores, one for  
173 sedimentary characteristics and radiocarbon data, the other in black photo-resistant liner for  
174 Optically Stimulated Luminescence dating (OLS) for a subsequent study. Each whole core  
175 was scanned using a CT (Computed Tomography) scanner to view internal sedimentary  
176 structures, while split core sections were photographed.

### 177 *3.3 Grain size analysis*

178 Four sediment cores were sampled for grain size analysis, which was conducted using a  
179 CILAS 1190L particle size analyzer following the methods of Sperazza et al. (2004). Cores  
180 HF-1, HF-3, and HF-7 were sampled at 5 cm intervals, excluding shell hash beds, where the  
181 particle size (>2500  $\mu\text{m}$ ) was too large for the instrument. HF-5, the longest core, was  
182 sampled at 2 cm intervals. The 1  $\text{cm}^3$  samples were pre-treated with 30% hydrogen peroxide  
183 ( $\text{H}_2\text{O}_2$ ) to remove organic material. Quantification of shell material was performed by pre-  
184 weighing dried 1  $\text{cm}^3$  samples collected at intervals of 10 cm, treating them with 10% HCl,  
185 and weighing after the reaction was carried out.



186        *3.4 Radiocarbon dating*

187        A total of 30 samples were collected for radiocarbon dating. Of these, 23 were gastropod  
188 shells, one was a bivalve, and six were wood fragments. The bivalve was articulated and only  
189 gastropods that showed no evidence of reworking, such as abrasion or fragmentation, were  
190 sampled. The species of the gastropods were also used to assess their habitat. Radiocarbon  
191 ages were measured using atomic mass spectrometry (AMS) at the University of California  
192 Irvine Keck carbon cycle accelerator mass spectrometer (KCCAMS) facility. Radiocarbon  
193 ages obtained from shells were calibrated using the Marine 20 calibration curve of (Heaton et  
194 al., 2020), while wood fragments were calibrated using the Intcal calibration curve of  
195 (Reimer et al., 2020) within the Calib 8.2 program (Stuiver et al., 2022).

196        **4. Results**

197        *4.1 Sedimentary facies*

198        Sediments collected from the CHS consist of silt, very fine sand, and fine sand (average  
199 grain sizes ranging from 80 – 130  $\mu\text{m}$ ) (Fig. 3). All sedimentary facies contain shell  
200 fragments, which range in size from 0.2 mm to 5 cm, and several of the facies contain  
201 articulated bivalves and well-preserved, intact gastropods. Mean sand content ranges from  
202 70% to 40%, with <10% clay found in all samples, and a varying proportion of shell  
203 fragments, depending on the sedimentary facies. Four sedimentary facies were identified  
204 within the CHS sediment cores: black sand facies, parallel and ripple cross laminated sand  
205 facies, sandy shell hash facies, and a sandy silt facies (Figs. 4, 5). Grain-size distributions for  
206 each sample aided in differentiating between the facies and in identifying subtle grain-size  
207 trends. A total of 30 radiocarbon ages were obtained from 24 shells and six wood fragments  
208 in the cores from the CHS (table 2). Ages range from modern to 12,195 cal. years B.P. Only  
209 three ages in core HF-5 obtained from a 36-mg wood fragment (HF-5, 115 cm), a 20-mg

210 wood fragment (HF-5, 287 cm) and a gastropod shell are out of sequence. Core HF-1 has one  
211 out of sequence date, which was obtained from a 30-mg wood fragment.

212 ***Black sand facies:*** The black sand facies appears in the lower portion of sediment cores  
213 HF-1, HF-7, and HF-4, as well as in the cutter nose of HF-3, which samples the seismic unit  
214 below the base of the CHS, package S<sub>1</sub> (Figs. 5, 6, 7). This facies is composed of clean fine-  
215 grained sand (average grain size 130  $\mu\text{m}$ ), with less than 5% silt and no clay. It has a  
216 unimodal grain-size and no skewness (Fig. 3). Shell fragments are scarce, comprising < 5%  
217 carbonate by weight. The namesake “black” color of this facies is due to the local Franciscan  
218 Complex sediment source area. Prominent rock types within the Franciscan Complex include  
219 sandstone, graywacke, conglomerate, greenstone, diabase, chert, serpentinite and  
220 glaucophane schist. Thus, sands sourced from it are rich in heavy minerals, including  
221 amphibole, pyroxene, epidote, sphene and magnetite. This mineral assemblage contrasts with  
222 the overlying brown shelf deposits, which have a lower portion of heavy minerals and higher  
223 proportion of shell fragments. In core HF-7, the black sand facies is comprised of two beds: a  
224 lower 20 cm-thick bed with parallel laminations and intact gastropods and an upper 13 cm-  
225 thick bed with no visible structures (Fig. 4a). The upper bed fines upward from fine to very  
226 fine sand (130  $\mu\text{m}$  to 110  $\mu\text{m}$ ). The fauna identified in this facies includes the two species  
227 *Clathurella canfieldi* and *Truncatella californica*. Both of these species prefer a sandy  
228 habitat, among surf grass roots in the upper intertidal zone (Guz, 2007). Radiocarbon dates  
229 from gastropods within this facies yield ages between 12,195-9,524 cal. years B.P. (table 2).

230 ***Parallel- and ripple-cross laminated sand:*** This facies occurs in cores HF-1, HF-3 and  
231 HF-5, but is not found in nearby core HF-7 collected seaward of the CHS (Figs. 1, 5). This  
232 facies is composed of very fine sand (mean grain size 90  $\mu\text{m}$ ) with an average abundance of  
233 50% sand, 40% silt, and 10% clay, as well as abundant shell fragments (~20% carbonate by  
234 weight). The grain size mode is 100  $\mu\text{m}$  and the grain-size distribution is negatively skewed

235 (Fig. 3). The parallel and ripple cross laminated facies is composed of 10 - 20 cm-thick  
236 inversely graded (100  $\mu\text{m}$  - 90  $\mu\text{m}$ ) to normally graded beds (90  $\mu\text{m}$  to 60  $\mu\text{m}$ ). The inverse  
237 graded beds sit atop an erosive base; however, these are only preserved in cores HF-3 and  
238 HF-5. Within the inversely graded beds, faint ripple-cross laminations are observed, and  
239 whole gastropod shells are abundant, ranging in size from 0.5 to 2 cm (Fig. 4b). Within the  
240 fining upward sequences, there is a marked alternation of parallel laminations and ripple-  
241 cross laminations every  $\sim$ 5 cm. Commonly, this facies is capped by alternating very fine sand  
242 and silt laminae (Fig. 4c). The shell fragments, while present throughout the facies, are more  
243 concentrated at the base of the beds. The fauna present in this facies consists of two main  
244 species: *Callianax baetica* and *Amphissa versicolor*. *Callianax baetica* mainly inhabits sandy  
245 or muddy substrates in offshore areas in water depths of up to 65 m and is rarely found in  
246 intertidal areas (Sept, 2019). *Amphissa versicolor* is common to the upper sections of the  
247 sediment cores, within the parallel and ripple cross laminated sand facies. It only inhabits  
248 subtidal areas up to  $\sim$ 50 m depths and can adapt to many types of substrates (rocky or  
249 muddy) (Austin, 1985; Gotshall, 1994; Guz, 2007; Sept, 2019). Radiocarbon dates from  
250 gastropods and wood fragments within this facies yield ages ranging between  $\sim$ 7,500 – 900  
251 cal years B.P. (table 2).

252 ***Sandy shell hash facies:*** This facies overlies the parallel and ripple cross laminated  
253 facies in cores HF-3 and HF-5, but is not present in cores HF-1 and HF-7 (Fig. 5). The sandy  
254 shell hash facies is composed of as many as five shell beds, almost entirely composed pebble  
255 sized shell fragments (ranging from 1 to 5 cm, on average 28-32% carbonate by weight) and  
256 fine to medium sand (300-500  $\mu\text{m}$ ). The individual shell hash beds are typically about 2 cm  
257 thick and are interbedded with  $\sim$  2 cm thick beds of medium and fine parallel laminated sands  
258 (Fig. 4d). The matrix (non-shelly component) grain size is unimodal and has no skewness,  
259 with a mode at 330  $\mu\text{m}$  (Fig. 3). The thickness and shell content of this facies decreases

260 basinward from 85 cm in core HF-5 (shell fragment content of 32% by mass) to 30 cm, in  
261 core HF-3 (shell fragment content of 24% by mass). Fauna in this facies is challenging to  
262 identify, as it is mainly composed of fragmented bivalve or gastropod shells. When intact  
263 gastropods are present, the most abundant species is *Amphissa versicolor*. Because of the  
264 lack of abundance of intact gastropods, only one radiocarbon date was obtained for this facies  
265 (from a *Amphissa versicolor* shell), yielding an age of 721-515 cal. years B.P. (table 2).

266 ***Sandy silt facies:*** The sandy silt facies comprises the top layer of all sediment cores (Fig.  
267 5). The average grain size is 40  $\mu\text{m}$  and it is composed of, on average, 65% silt, 30% sand,  
268 and 5% clay. The grain-size distribution is polymodal, with peaks at 100  $\mu\text{m}$ , 50  $\mu\text{m}$  and 30  
269  $\mu\text{m}$  (Fig. 3). No visible sedimentary structures other than burrowing were observed within the  
270 beds, and they contain fewer (~7% carbonate mass by weight) scattered shell fragments (0.2  
271 mm) compared to the other facies found in the cores (Fig. 4e). Fauna in this facies is rarely  
272 present, but occasional *Amphissa versicolor* are identified. Radiocarbon dating from  
273 gastropod shells within this facies yield modern ages (table 2).

274

#### 275 4.2 Seismic-reflection profiles

276 The chirp data across the CHS reveal the presence of three distinct seismic units:  $S_1$ ,  $S_2$ ,  
277 and  $S_3$  (Figs. 6, 7). Seismic unit  $S_1$  is the lowest of the identified units and is marked by  
278 weakly developed divergent, high amplitude, chaotic reflections with occasional reflection-  
279 free zones. This unit is found below and seaward of the CHS. Seismic unit  $S_2$  overlies  $S_1$ , and  
280 is characterized by medium amplitude, basin dipping sigmoidal reflections. This unit pinches  
281 out at the bottomset of the CHS. Reflections in seismic unit  $S_2$  are truncated against seismic  
282 unit  $S_3$ , which is distinguishable by its scoop shape and its high amplitude, subparallel  
283 reflections. This unit is not continuous through the clinoformal feature but rather develops as  
284 the fill of scour features scattered across the top of the CHS (Figs. 6, 7).

## 285 **5. Facies Interpretation**

286           The main body of the CHS, is composed of the parallel and ripple cross-laminated  
287 sand facies, which corresponds to seismic unit S<sub>2</sub>. Seismic unit S<sub>2</sub> progrades over seismic unit  
288 S<sub>1</sub>, which is comprised of the black sand facies, representing an older Younger Dryas stadial  
289 shoreface. Progradation of the CHS was promoted by a slowdown in the rate of RSL rise  
290 (Reynolds and Simms, 2015), an optimal condition for the formation of subaqueous  
291 prograding bodies, as sediment supply to the shelf area outpaces the rate of sea-level rise  
292 (Hernandez-Molina et al., 2000; Patruno et al., 2015; Patruno & Helland-Hansen, 2018;  
293 Budillon et al., 2022). Seismic unit S<sub>3</sub>, which corresponds to the sandy shell hash facies,  
294 represents a younger erosive feature that has scoured and filled the clinoformal sediments  
295 with coarse grained (up to 5 cm) shell fragments and medium sands. The sandy silt facies  
296 most likely corresponds to the top of seismic unit S<sub>2</sub> and, where present, unit S<sub>3</sub>. However,  
297 this contact is not discernable in the chirp data. Below we discuss each sedimentary facies  
298 and their role in building the subaqueous clinoform.

299           ***Black sand facies:*** The oldest sediment observed in our cores is the black sand facies,  
300 which corresponds to seismic unit S<sub>1</sub>. The seismic character, typical of shoreface deposits,  
301 and the well-sorted fine sand with parallel laminations and unimodal grain-size distribution of  
302 the black sand facies suggest deposition may have occurred within a lower to upper shoreface  
303 environment, where waves and currents are the principal mechanism of sediment transport  
304 (Niedoroda et al., 1984) and able to winnow the finer sediments, resulting in well sorted,  
305 parallel laminated sands (table 3). The *Clathurella canfieldi* and *Truncatella californica*  
306 gastropods that are only found within the black sand facies prefer an upper intertidal habitat  
307 in sandy bottoms, which suggest deposition in a shallower marine environment. Ages from  
308 this deposit correspond to the Younger Dryas interstadial (Table 2). During this time RSL in  
309 southern California is estimated to have been between -55 and -60 m (Reynolds and Simms,

2015; Yousefi et al., 2018). Considering cores HF-1 and HF-7 were collected in water depths of 82 and 81 m, respectively, we interpret the black sand facies as a unit deposited in much shallower water depths than present (less than 20 m) (Fig. 2). The post Younger Dryas ages obtained within this facies range from 10,035-9,524 cal. years B.P. (Table 2). The gastropods used for dating in this case were sampled from the top of the black sand facies, and were most likely subjected to post Younger Dryas reworking, such as draping, and bio-occupation.

The black sand facies is separated from the parallel and ripple cross laminated facies by a sharp erosive contact, and a < 2 cm thick bed of shell fragments (Fig. 5). This contact is always observed above the black sand facies, including cores HF-1, HF-4 and HF-7. Considering the missing time between the black sand facies and the parallel and ripple cross laminated facies, as well as the erosive nature of their contact, we interpret this contact as a wave ravinement surface (WRS). WRSs are commonly sculpted by waves during transgression and are often mantled by shell lag deposits (Cattaneo and Steel, 2003; Zecchin et al., 2019), much like the shell layer observed above the black sand facies. We propose that rapid sea-level rise post-dating the Younger Dryas stadial emplaced the shell lag deposit above the now relict shoreface deposit, represented by the black sand facies.

***Parallel and ripple cross laminated sand facies:*** The parallel and ripple-cross laminated sand facies comprises seismic unit S<sub>2</sub>, which pinches out at the foot of the CHS (Fig. 6). Based on the correlation between the cores and seismic profiles (Figs. 5, 6), the parallel and ripple cross laminated facies dominates the main prograding body of the CHS. Strata are organized in ~10 - 30 cm-thick beds, each of which displays an erosive base, overlain by inversely to normally graded beds that transition to a parallel and ripple cross laminated fining upward unit. Shell fragments are prevalent throughout the beds, amounting to 20 - 25% carbonate by weight, while wood material is rare. Siliciclastic sediment is thoroughly mixed with the shell fragments, indicating sediment mixing and minor amounts of

335 wood further support possible offshore transport by intrabasinal processes such as waves and  
336 tides. Taken together, these beds are consistent with deposition by turbulent flows,  
337 transitioning between upper- and lower-flow regimes, capable of producing parallel  
338 laminations and grading into ripple cross lamination as a result of traction and fallout  
339 processes (Sanders, 1960) (table 3). The slightly coarser grain sizes and inverse grading result  
340 from dispersive pressures and a lag in transport of the coarser material (Hand, 1997). The  
341 transition between the inverse graded and the normally graded sequences may represent the  
342 ‘maximum’ waxing of the flow (Mulder et al., 2003). As the flow loses velocity, a fining  
343 upward unit is deposited, marked by an alternation of parallel laminations and ripple-cross  
344 laminations. The top of the deposit fines upward to silty beds, which are often intercalated  
345 with thin laminae of very fine sand. We interpret these silts as the fine-grained, late-stage  
346 suspension deposits associated with some sort of sediment gravity flow.

347 Radiocarbon ages from the parallel and ripple cross laminated facies (seismic unit S<sub>2</sub>)  
348 suggest that deposition occurred between 7,088 – 6,749 cal. years B.P. (maximum age of  
349 deposition; Table 2) and 1,157-898 cal. years B.P. During this time period, RSL along  
350 California is estimated to be ~ 6.5 m bsl, and ~0.5 m bsl, respectively (Reynolds and Simms,  
351 2015, Fig. 2) placing the CHS in water depths ranging between ~ 63.5 m and ~ 69.5 m at the  
352 time of deposition (Fig. 2). Additionally, the fauna identified within the CHS further suggests  
353 deposition in deeper water, as both *Callianax baetica* and *Amphissa versicolor* prefer a  
354 subtidal habitat, in water depths of up to 65 m (Austin, 1985; Gotshall, 1994; Sept, 2019).

355 ***Sandy shell hash facies:*** The sandy shell hash facies is found in cores sampling  
356 seismic unit S<sub>3</sub>. Seismic unit S<sub>3</sub> has an irregular erosional base that appears to represent  
357 scour into the underlying sediment of seismic unit S<sub>2</sub>. Unit S<sub>3</sub>, comprised of the sandy shell  
358 hash facies, is not laterally continuous through the CHS, but rather organized in localized  
359 ‘pockets’ (Figs. 6, 7). The basinward extent of this unit is less than that of the parallel and

360 ripple cross laminated sand facies, pinching out between core HF-3 and HF-1 (Fig. 5). This  
361 facies is coarser and richer in biogenic material (medium sand and shell fragments up to 5  
362 cm) than the parallel and ripple cross laminated facies. Based on the unimodal, coarsely  
363 skewed grain size distribution (GSD) of the sandy shell hash facies and the presence of large  
364 shell fragments and parallel laminations, we invoke strong wave action as responsible for the  
365 suspension, reworking, and seaward advection of the sediment, where the coarser material is  
366 eventually separated from its finer particles, leaving behind a coarsely skewed, shelly deposit  
367 (Table 3) (Hernandez-Molina et al., 2000; Zecchin et al., 2019). The sandy shell hash facies  
368 is most likely not genetically linked to the flow deposits, but rather represents a younger  
369 storm deposit that scoured into the clinoformal sediment.

370 ***Sandy silt facies:*** The sandy silt facies, which blankets the CHS, is most likely not  
371 genetically linked to the flows feeding the progradation of the CHS. This sedimentary facies  
372 is not visible in the seismic data and cannot be grouped into one seismic package. However,  
373 the sandy silt facies is found in cores throughout the CHS (topset, foreset, bottomset) and it  
374 maintains a near uniform thickness, and does not pinch out in deeper water depths as does the  
375 parallel and ripple cross laminated facies (Fig. 5). It post-dates ~700 years B.P. and is thus  
376 interpreted to represent modern day hemipelagic accumulation and is similar to sediment at  
377 the top of some of the fining-upward sequences in the underlying parallel and ripple cross  
378 laminated facies.

## 379 **6. Discussion**

### 380 *6.1 Genesis and evolution of the Cross Hosgri Slope*

381 In chirp profiles the CHS resembles the infralittoral prograding wedges (IPW) of  
382 Hernandez-Molina et al. (2000) recently reviewed by Budillon et al. (2022), displaying thin  
383 topsets with high acoustic reflectivity and foresets with seaward dipping, high amplitude  
384 reflections. They describe IPWs as depositional bodies defined by internal clinoforms and



385 whose main mechanism of progradation is dictated by storm waves. Here we explore the  
386 driving mechanisms of progradation for the CHS and, by analogy, other IPWs.

387         Given the absence of a fluvial source other than the relatively small (123 km<sup>2</sup>) Santa  
388 Rosa watershed located about 10 km north of the CHS, fluvial-deltaic sediment transport is  
389 likely not a viable mechanism for driving CHS progradation. However, the central California  
390 shelf is characterized by a high energy wave climate, specifically in the winter months, when  
391 wave activity associated with storms is greatest (Dingler et al., 1982; Storlazzi and Griggs,  
392 2000; Storlazzi and Wingfield, 2005). We propose that intense wave action entrained and  
393 mobilized sandy and silty shelf sediment and shell fragments, which were swept to the  
394 seaward edge of the topset of the CHS where that sediment fed WSGFs that prograded the  
395 CHS. A break in slope given by the relict shoreface beneath the CHS (seismic unit S1, black  
396 sand facies) allowed for a nucleation point to build the initial clinof orm geometry of the CHS.

397         To explore the possible role of WSGFs in the growth of the CHS, we examine the two  
398 dominant factors that contribute to these flows: the slope of the seafloor, and wave influence.  
399 Wright et al. (2001) showed that gravity currents can only be sustained at a minimum slope,  
400 defined by:

$$401 \quad \sin\theta = (C_d / Ri_{cr}) (|u| / u_g) \quad (1)$$

402 where  $C_d$  is the bottom drag coefficient,  $Ri_{cr}$  is the critical Richardson number,  $|u|$  represents  
403 the velocity scale related to friction on the gravity current, and  $u_g$  is the speed of the gravity  
404 current. While  $Ri$  numbers as small as 0.01 have been suggested for sandy environments as  
405 in the case of predominantly medium sands of Flores et al. (2018), we use the widely  
406 accepted  $Ri_{cr} = 0.25$  and  $C_d \sim 0.003$  usually applied to finer sediments (silt and clay) (Scully  
407 et al., 2003; Wright et al., 2001), as the sediment comprising the prograding portion of the  
408 CHS is on average 50% very fine sand, 40% silt, and 10% clay. In a scenario with no wave  
409 influence,  $|u|$  equals  $u_g$  in equation (1), and the minimum slope to sustain gravity currents

410 corresponds to  $0.7^\circ$  (Wright and Friedrichs, 2006; Wright et al., 2001). The slope of the beds  
411 below the CHS (seismic unit S<sub>1</sub>, Fig. 6) is  $1.3^\circ$ , suggesting sustained movement of a wave-  
412 supported gravity flow is possible at the location of the CHS. However, the shelf slope  
413 seaward and landward of the CHS varies between  $0.4^\circ - 0.6^\circ$  (Johnson et al., 2014), a value  
414 below the minimum threshold for downslope gravity movement.

415 Wave influence along the wave-dominated California shelf must, however, be taken  
416 into account when using equation (1). In this scenario,  $|u| > u_g$  in equation (1), suggesting that  
417 sediment suspension increases, promoting sediment flows at shelf slopes shallower than  $0.7^\circ$   
418 (Wright et al., 2001). We explore this possibility by using average wave period and  
419 significant wave height to estimate the necessary conditions of orbital wave velocities to  
420 entrain sediments at depth. By calculating the maximum orbital velocity obtained by swell  
421 waves, Porter-Smith et al. (2004) showed that when near bed currents accelerate from zero to  
422 a maximum value, they may exceed the threshold value where a specific grain size can be  
423 mobilized. Using Porter-Smith et al. (2004):

$$424 \quad U_{\max} = (\pi H) / [T \sinh(2 \pi h / \lambda)] \quad (2)$$

425 where H represents the wave height, h is the water depth, and  $\lambda$  is the wavelength (Porter-  
426 Smith et al., 2004). The critical threshold for grain movement suggested by Clifton and  
427 Dingler (1984) is:

$$428 \quad U_{\text{cr}} = 33.3(TD)^{0.33} \quad (3)$$

429 where T is the wave period, and D is the grain diameter. If the maximum velocity of the  
430 waves ( $U_{\max}$ ) exceeds the threshold speed ( $U_{\text{cr}}$ ), then mobilizing sediment with a grain  
431 diameter of D will be possible (Porter-Smith et al., 2004). We solve for  $U_{\max}$  under both  
432 winter and summer conditions in central California, using data from the National Data Buoy  
433 Center of the NOAA.gov database (station ID: 46028, fig. 1b) for the years between 1983-

2010. At this time, constraints on paleo-wave conditions for the Holocene along central California are limited. As climatic conditions have not significantly changed in the last 7 ka in central California (Dupre, 1983, Kirby et al., 2005), this allows for present day wave statistics to be used in this study. We find that under winter swell conditions,  $U_{\max}$  exceeds  $U_{\text{cr}}$  for a grain diameter of 90  $\mu\text{m}$  (mean grain size in the parallel and ripple cross laminated facies) in 10% of the cases at a depth of 70 m (Figs. 8, 9). However, these conditions for sediment remobilization are obtained less often at 85 m depth, where remobilization occurs in < 2% of the cases (Figs. 8, 9). These observations suggest remobilization of the sediment is possible under winter swell conditions at the topset of the CHS (70 m water depth), while it is less likely to occur basinward of the foot of the CHS (~85 m water depth). In the case of summer swell conditions,  $U_{\max}$  rarely exceeds  $U_{\text{cr}}$  (ensuing only 0.2% of the times, at the topset of the CHS, and 0.001% of the times at the foot of the CHS; Figs. 8, 9), suggesting remobilization of the sediment by swell waves is not common under fair-weather conditions. While we recognize that  $U_{\max}$  could be affected by currents in the area, we treat wave action as the main contributor to  $U_{\max}$ , as the two largest currents in this region, the California Current and the Davidson Current do not appear capable of entraining sediment of the size comprising the CHS. The California Current flows at the shelf edge and extends up to 200 km from the coast. Even at the surface, where it maintains its highest speeds, its velocity of 0.05 m/s is too low to remobilize sediments of the size comprising the CHS (Aquad et al., 2011) (Eq. 2, 3). The Davidson Current, while closer to shore, is weaker than the California Current, and flows northward (Checkley and Barth, 2009; Reid and Schwartzlose, 1962), the opposite direction of the south-west progradation of the CHS. We suggest the progradation of the CHS is promoted by intense winter storm waves, which are capable of moving very fine sand grains at water depths up to ~70 m. An increase in shelf gradient (from 0.4° to 1.3°) given by a relict shoreface (black sand facies) acts as a nucleation point for clinoform

460 progradation. Here WSGFs are initiated, which travel over the rollover point, and  
461 consequently cascade over the foreset promoting clinoform progradation. Without sustained  
462 waves and a low shelf gradient at the bottom set ( $0.4^\circ$ ) they cannot travel beyond the toe of  
463 the foreset. During fair weather conditions, fine silts and clays of the sandy silt facies settle  
464 out onto the seafloor. We suggest the sandy silt facies only accumulates in between large  
465 storms, and once WSGFs are triggered by extreme events, these finer sediments are eroded  
466 and/or reworked into the flows.

467         Progradation of the CHS seems to have stopped, or paused around 0.7 ka. We are not  
468 certain as to why deposition stopped, as conditions appear to be favorable for their  
469 development given today's wave climate. One possibility for the break in WSGF activation  
470 may be a large storm event(s) that simultaneously emplaced the sandy shell hash facies  
471 (forming scours in the CHS) and removed all fine materials from the source area. As a result,  
472 triggering of WSGFs may have been interrupted as a result of a limited supply of fine  
473 sediment that has yet to recover from the event.

474         The environmental setting of the CHS can be used as a guideline for establishing the  
475 conditions necessary for the formation of subaqueous clinoforms built by WSGFs.  
476 Clinoformal sediment accumulation require high enough wave energy to suspend sand at the  
477 seafloor. In the case of the CHS in  $\sim 70$  m water depth, significant wave heights need to  
478 exceed  $\sim 4$  m with wave periods of  $\sim 10$  seconds to mobilize very fine sand. While waves are  
479 a crucial component to initializing WSGFs, a steep enough shelf gradient is required to  
480 promote sustained gravity flows. Any steep gradient shelf ( $> 0.7^\circ$ ) with a high energy wave  
481 climate is considered to be an ideal framework to produce WSGFs. Alternatively, on gentler  
482 shelves, a zone of high relief on the seafloor (produced by tectonic activity, or a  
483 paleoshoreline) can also act as a nucleation point for clinoform growth by WSGFs. Thus, it is  
484 likely that subaqueous clinoforms built by WSGFs can occur along any shelf, even sediment

485 starved areas such as the shelf north of Estero Bay, pending the right wave regime and shelf  
486 gradient. Shelf subaqueous clinoforms, specifically when formed by WSGFs in the absence  
487 of direct fluvial input, demonstrate that continental shelves are dynamic environments rather  
488 than a zone of bypass, and that it is possible for sediment accumulation to occur even during  
489 a sea-level highstand.

490 One intriguing hypothesis concerning the gravity flows comprising the CHS involves  
491 tectonic activity. The CHS is cut by the Hosgri fault, an active Holocene structure with a  
492 proposed slip rate of  $2\pm 0.9$  mm/yr (Johnson et al., 2014). Sediment gravity flows can be  
493 triggered by earthquakes (e.g., along the Cascadia Subduction Zone) (Goldfinger et al., 2003)  
494 thus, each of the turbulent sediment flow units may represent a significant ground-shaking  
495 event. However, following a seismic triggered sediment failure a scar on the seafloor should  
496 be visible, and none is visualized in the bathymetry data from Johnson et al. (2014).  
497 Furthermore, without an independent record of earthquakes on the Hosgri fault it is not  
498 possible to test this hypothesis at the current time.

## 499 *6.2 Similar shelf features*

500 Several bathymetric features along the central California shelf have been mapped and  
501 described as prograding latest Pleistocene and Holocene sediment bars (Johnson et al., 2019),  
502 only some of which are adjacent to the mouths of significant coastal watersheds. These  
503 features have similar orientations and scales as the CHS, and occur at water depths  $\sim 50$  m.  
504 Given these observations, WSGF-built subaqueous clinoforms are likely more widespread  
505 along the central California shelf. Similar features, such as IPWs, have been mapped across  
506 the Italian peninsula and other places in the Mediterranean (Budillon et al., 2022; Hernandez-  
507 Molina et al., 2000), but few have been cored or sampled.

## 508 *6.3 A facies model for sandy wave-supported gravity flows and associated* 509 *subaqueous clinoforms*

510 Our analysis of the sedimentary facies near the CHS allows us to propose a facies  
511 model for a subaqueous clinoform, or an IPW, composed of sandy WSGF deposits (Fig. 10).  
512 The parallel and ripple cross laminated facies is deposited by the WSGF building the  
513 subaqueous clinoform. The WSGF deposits are characterized by an erosive base indicating  
514 emplacement by a turbulent flow. Above the erosive base, is an inversely graded bed with  
515 abundant shell fragments and fine to medium sands from the most energetic parts of the flow,  
516 where bedload is deposited as inverse grading as a result of the lag in transport of the coarser  
517 material (Hand, 1997). As the peak of the flow passes, the energy decreases as the turbulent  
518 flow oscillates between upper- and lower-flow regimes, producing alternating parallel and  
519 ripple cross laminated beds of very fine sands. The transition between reverse and normal  
520 grading as well as the alternation between parallel and ripple cross laminations indicates a  
521 waxing and waning of the flow. The alternations in the flow are most likely due to temporal  
522 changes in wave intensity. Finally, an increase in the fallout rate as the flow begins to  
523 dissipate causes deposition of the suspended load, emplacing a silt cap at the top of the beds  
524 (Fig. 10). These deposits are similar to the ‘wave modified turbidites’ sourced by  
525 hyperpycnal flows as described by Lamb et al., (2008). However, in our scenario the gravity  
526 flow is triggered by wave action itself rather than following a river flood, and later sustained  
527 by an increase in the shelf slope.

## 528 **7. Conclusions**

529 Chirp data, sediment cores, and radiocarbon ages are used to describe the age and origin  
530 of a wave-supported gravity flow (WSGF)-built subaqueous clinoform – or Infralittoral  
531 Prograding Wedges (IPW), sensu Hernandez-Molina et al., (2000) – along the central  
532 California shelf locally known as the Cross Hosgri Slope (CHS). In the absence of sediment  
533 cores, the CHS had previously been interpreted to be a drowned shoreface paired to a now  
534 eroded sandspit (Johnson et al., 2014). While the presence of a drowned shoreface is also

535 identified in this study, we find that a subaqueous clinoform nucleated atop the relict  
536 shoreface. Its mode of progradation was set up by winter swell waves remobilizing shelf  
537 sediment and sweeping them across the seafloor until they reached a break in slope, provided  
538 by the relict shoreface, where the finer sediments transitioned into sediment gravity flows  
539 leaving behind several fining upward beds marked by sedimentary structures indicative of  
540 pulsating flows. We suggest that WSGFs can form in sandy environments and do not  
541 necessarily need to be triggered by or sourced from river floods. We propose a facies model  
542 for sandy WSGF deposits, characterized by an erosive base, a sandy coarsening upward bed,  
543 followed by very fine sands marked by parallel and ripple cross lamination, and capped by  
544 interbedded very fine sands and silts (Fig. 10). Furthermore, this study provides a model for  
545 the formation of subaqueous clinoforms that occur in isolation and whose feeding mechanism  
546 mainly relies on winter swell. Their proper identification as subaqueous sandy bodies is  
547 important as to distinguish them from low stand deposits (Patruno et al., 2015; Peng et al.,  
548 2020).

## 549 **8. Data Availability**

550 Datasets related to this article can be found at <https://doi.org/10.5066/P9A0U8J7>, an open-  
551 source online data repository hosted by the USGS (Snyder et al., 2022).

552

## 553 **Acknowledgements**

554 This work was funded through a gift from Pacific Gas and Electric (PG&E), as well as a  
555 grant from the U.S. Geological Survey (USGS) National Earthquake Hazard Reduction  
556 Program (NEHRP) grant number G20AS00042 to University of California Santa Barbara.  
557 We also thank the captain and crew of the M/V *Bold Horizon*, John Southon and Chanda  
558 Bertrand at University of California Irvine for their help with radiocarbon dating, as well as

559 Vanessa Delnavaz at Santa Barbara Museum of Natural History for her help with shell  
560 identification. Any use of trade, product, or firm names is for descriptive purposes only and  
561 does not imply endorsement by the U.S. Government.

562  
563 **Bibliography**

564 Auad, G., Roemmich, D., Gilson, J., 2011. The California Current System in relation to the  
565 Northeast Pacific Ocean circulation. *Progress in Oceanography* 91, 576–592.  
566 <https://doi.org/10.1016/j.pocean.2011.09.004>

567 Austin, W.C., 1985. An Annotated Checklist of Marine Invertebrates in the Cold Temperate  
568 Northeast Pacific. Khoyatan Marine Laboratory.

569 Bakker, E., Slack, G., 1985. *An Island Called California: An Ecological Introduction to Its*  
570 *Natural Communities, Revised and Expanded*, 2nd ed. Univ of California press.

571 Bray, N.A., Keyes, A., Morawitz, W.M.L., 1999. The California Current system in the  
572 Southern California Bight and the Santa Barbara channel. *Journal of Geophysical*  
573 *Research-Oceans* 104, 7695–7714. <https://doi.org/10.1029/1998jc900038>

574 Budillon, F., Amodio, S., Alberico, I., Contestabile, P., Vacchi, M., Innangi, S., Molisso, F.,  
575 2022. Present-day infralittoral prograding wedges (IPWs) in Central-Eastern Tyrrhenian  
576 Sea: Critical issues and challenges to their use as geomorphological indicators of sea  
577 level. *Marine Geology*. <https://doi.org/10.1016/j.margeo.2022.106821>

578 California State University Monterey Bay Sea Floor Mapping Lab (CSUMB) (2012).  
579 Seafloor Mapping Lab at CSUMG, [http://seafloor.csumb.edu/SFMLwebDATA\\_c.htm](http://seafloor.csumb.edu/SFMLwebDATA_c.htm)

580 Cattaneo, A., Steel, R.J., 2003. Transgressive deposits: a review of their variability. *Earth-*  
581 *Science Reviews* 62, 187–228. [https://doi.org/10.1016/S0012-8252\(02\)00134-4](https://doi.org/10.1016/S0012-8252(02)00134-4)

582 Checkley, D.M., Barth, J.A., 2009. Patterns and processes in the California Current System.  
583 *Progress in Oceanography* 83, 49–64. <https://doi.org/10.1016/j.pocean.2009.07.028>

584 Chelton, D.B., 1984. Seasonal variability of alongshore geostrophic velocity off central  
585 California. *Journal of Geophysical Research* 89, 3473.  
586 <https://doi.org/10.1029/JC089iC03p03473>

587 Clark, J.A., Farrell, W.E., Peltier, W.R., 1978. Global Changes in Post-Glacial Sea-Level -  
588 Numerical-Calculation. *Quaternary Research* 9, 265–287. [https://doi.org/10.1016/0033-5894\(78\)90033-9](https://doi.org/10.1016/0033-5894(78)90033-9)

590 Clifton, H., Dingler, J., 1984. Wave-formed structures and paleoenvironmental  
591 reconstruction. [https://doi.org/10.1016/0025-3227\(84\)90149-X](https://doi.org/10.1016/0025-3227(84)90149-X)

592 Collins, C.A., Pennington, J.T., Castro, C.G., Rago, T.A., Chavez, F.P., 2003. The California  
593 Current system off Monterey, California: physical and biological coupling. *Deep-Sea*  
594 *Research Part II-Topical Studies in Oceanography* 50, 2389–2404.  
595 [https://doi.org/10.1016/S0967-0645\(03\)00134-6](https://doi.org/10.1016/S0967-0645(03)00134-6)



596 Dickinson, W.R., Ducea, M., Rosenberg, L.I., Greene, H.G., Graham, S.A., Clark, J.C.,  
597 Weber, G.E., Kidder, S., Ernst, W.G., Brabb, E.E., 2005. Net Dextral Slip, Neogene San  
598 Gregorio-Hosgri Fault Zone, Coastal California: Geologic Evidence and Tectonic  
599 Implications, Net Dextral Slip, Neogene San Gregorio-Hosgri Fault Zone, Coastal  
600 California: Geologic Evidence and Tectonic Implications. Geological Society of  
601 America. <https://doi.org/10.1130/spe391>

602 Dingler, J.R., Anima, R.J., Molzan, D.E., Luepke, G., Peterson, C.L., 1982. A field study of  
603 littoral processes in Estero Bay, California, Open-File Report. U.S. Geological Survey.

604 Dupré, W.R., 1984. Reconstruction of paleo-wave conditions during the late Pleistocene from  
605 marine terrace deposits, Monterey bay, California. *Developments in Sedimentology* 39,  
606 435-454. [https://doi.org/10.1016/S0070-4571\(08\)70158-4](https://doi.org/10.1016/S0070-4571(08)70158-4)

607 Fernández-Salas, L.M., Dabrio, C.J., Goy, J.L., Díaz del Río, V., Zazo, C., Lobo, F.J., Sanz,  
608 J.L., Lario, J., 2009. Land–sea correlation between Late Holocene coastal and  
609 infralittoral deposits in the SE Iberian Peninsula (Western Mediterranean).  
610 *Geomorphology* 104, 4–11. <https://doi.org/10.1016/j.geomorph.2008.05.013>

611 Flores, R.P., Rijnsburger, S., Meirelles, S., Horner-Devine, A.R., Souza, A.J., Pietrzak, J.D.,  
612 Henriquez, M., Reniers, A., 2018. Wave Generation of Gravity-Driven Sediment Flows  
613 on a Predominantly Sandy Seabed. *Geophysical Research Letters* 45, 7634–7645.  
614 <https://doi.org/10.1029/2018GL077936>

615 Goldfinger, C., Nelson, C.H., Johnson, J.E., 2003. Holocene earthquake records from the  
616 Cascadia subduction zone and northern San Andreas fault based on precise dating of  
617 offshore turbidites. *Annual Review of Earth and Planetary Sciences* 31, 555–577.  
618 <https://doi.org/10.1146/annurev.earth.31.100901.141246>

619 Gotshall, D., 1994. Guide to marine invertebrates: Alaska to Baja California. Sea  
620 Challengers, Monterey, California.

621 Guz, S.S., 2007. The light and smith manual: Intertidal invertebrates from central California  
622 to Oregon. *Library Journal* 132, 154.

623 Hand, B.M., 1997. Inverse grading resulting from coarse-sediment transport lag. *Journal of*  
624 *Sedimentary Research* 67, 124–129. <https://doi.org/10.1306/D426850E-2B26-11D7-8648000102C1865D>

626 Hanson, K.L., Lettis, W.R., McLaren, M., Savage, W., Hall, T.N., 1995. Style and Rate of  
627 Quaternary Deformation of the Hosgri Fault Zone, Offshore South-Central Coastal  
628 California.

629 Hartwell, S. R., D. P. Finlayson, P. Dartnell, and S. Y. Johnson (2013). Bathymetry and  
630 acoustic backscatter, Estero Bay, California, U.S. Geol. Surv. Open-File Rept. 2013-  
631 1225, <http://pubs.usgs.gov/of/2013/1225/abstract.html>

632 Hawley, R., Diggory, Z., Wald, S., 2012. Santa Rosa Creek watershed management plan.  
633 Prepared for the California Department of fish and game. California Department of fish  
634 and game 169.

- 635 Heaton, T.J., Köhler, P., Butzin, M., Bard, E., Reimer, R.W., Austin, W.E.N., Ramsey, C.B.,  
636 Grootes, P.M., Hughen, K.A., Kromer, B., Reimer, P.J., Adkins, J., Burke, A., Cook,  
637 M.S., Olsen, J., Skinner, L.C., 2020. Marine20—The Marine Radiocarbon Age  
638 Calibration Curve (0–55,000 cal BP). *Radiocarbon* 62, 779–820.  
639 <https://doi.org/10.1017/RDC.2020.68>
- 640 Hernandez-Molina, F.J., Fernandez-Salas, L.M., Lobo, F., Somoza, L., Diaz-del-Rio, V.,  
641 Alveirinho Dias, J.M., 2000. The infralittoral prograding wedge: a new large-scale  
642 progradational sedimentary body in shallow marine environments. *Geo-Marine Letters*  
643 20, 109–117. <https://doi.org/10.1007/s003670000040>
- 644 Hickey, B.M., 1998. Coastal oceanography of western North America, from the tip of Baja  
645 California to Vancouver Island. *The Sea* 11, 345–393, 1062.
- 646 Johnson, S.Y., Hartwell, S.R., Dartnell, P., 2014. Offset of Latest Pleistocene Shoreface  
647 Reveals Slip Rate on the Hosgri Strike-Slip Fault, Offshore Central California. *Bulletin*  
648 *of the Seismological Society of America* 104, 1650–1662.  
649 <https://doi.org/10.1785/0120130257>
- 650 Johnson, S.Y., Hartwell, S.R., Watt, J.T., Beeson, J.W., Dartnell, P., 2019. Offshore shallow  
651 structure and sediment distribution, Point Sur to Point Arguello, central California: U.S.  
652 Geological Survey Open-File Report 2018–1158, 3 sheets, scales 1:150,000 and  
653 1:200,000. <https://doi.org/https://doi.org/10.3133/ofr20181158>.
- 654 Johnson, S.Y., Watt, J., 2012. Influence of fault trend, bends, and convergence on shallow  
655 structure and geomorphology of the Hosgri strike-slip fault, offshore central California.  
656 *Geosphere*. <https://doi.org/10.1130/GES00830.1>
- 657 Johnson, S.Y., Watt, J.T., Hartwell, S.R., Kluesner, J.W., 2018. Neotectonics of the Big Sur  
658 Bend, San Gregorio-Hosgri Fault System, Central California. *Tectonics* 37, 1930–1954.  
659 <https://doi.org/10.1029/2017TC004724>
- 660 Kämpf, J., Chapman, P., 2016. The California Current Upwelling System, in: *Upwelling*  
661 *Systems of the World*. Springer International Publishing, Cham, pp. 97–160.
- 662 Kirby, M. E., Lund, S. P. and Poulsen, C. J. 2005. Hydrologic variability and the onset of  
663 modern El Niño–Southern Oscillation: a 19 250-year record from Lake Elsinore,  
664 southern California. *J. Quaternary Sci.*, Vol. 20 pp. 239–254. ISSN 0267-8179.
- 665 Lamb, M.P., Myrow, P.M., Lukens, C., Houck, K., Strauss, J., 2008. Deposits from Wave-  
666 Influenced Turbidity Currents: Pennsylvanian Minturn Formation, Colorado, U.S.A.  
667 *Journal of Sedimentary Research* 78, 480–498. <https://doi.org/10.2110/jsr.2008.052>
- 668 Langenheim, V.E., Jachens, R.C., Graymer, R.W., Colgan, J.P., Wentworth, C.M., Stanley,  
669 R.G., 2013. Fault geometry and cumulative offsets in the central Coast Ranges,  
670 California: Evidence for northward increasing slip along the San Gregorio–San Simeon–  
671 Hosgri fault. *Lithosphere* 5, 29–48. <https://doi.org/10.1130/L233.1>
- 672 Ma, Y., Wright, L.D., Friedrichs, C.T., 2008. Observations of sediment transport on the  
673 continental shelf off the mouth of the Waiapu River, New Zealand: Evidence for  
674 current-supported gravity flows. *Continental Shelf Research* 28, 516–532.  
675 <https://doi.org/10.1016/J.CSR.2007.11.001>

- 676 Martínez-Carreño, N., García-Gil, S., Cartelle, V., 2017. An unusual Holocene fan-shaped  
677 subaqueous prograding body at the back of the Cíes Islands ridge (Ría de Vigo, NW  
678 Spain): Geomorphology, facies and stratigraphic architecture. *Marine Geology* 385, 13–  
679 26. <https://doi.org/10.1016/J.MARGE0.2016.11.015>
- 680 Mitchell, N.C., 2012. Modeling The Rollovers of Sandy Clinofolds from the Gravity Effect  
681 On Wave-Agitated Sand. *Journal of Sedimentary Research* 82, 464–468.
- 682 Mulder, T., Syvitski, J.P.M., Migeon, S., Faugères, J., Savoye, B., 2003. Marine hyperpycnal  
683 flows: initiation, behavior and related deposits. A review. *Marine and Petroleum*  
684 *Geology* 20, 861–882. <https://doi.org/10.1016/j.marpetgeo.2003.01.003>
- 685 Niedoroda, A.W., Swift, D.J.P., Hopkins, T.S., Ma, C.-M., 1984. Shoreface Morphodynamics  
686 on Wave-Dominated Coasts, in: Greenwood, B., Davis, R.A. (Eds.), *Developments in*  
687 *Sedimentology*. Elsevier, pp. 331–354.
- 688 Nishenko, S., G. H, H., Hogan, P., Bergkamp, B., 2018. Geometry and Late Pleistocene  
689 Displacement of the Shoreline and Oceanic Fault Zones, San Luis Obispo Bay,  
690 California. *Bulletin of the Seismological Society of America*.  
691 <https://doi.org/10.1785/0120160177>
- 692 Ogston, A.S., Cacchione, D.A., Sternberg, R.W., Kineke, G.C., 2000. Observations of storm  
693 and river flood-driven sediment transport on the northern California continental shelf.  
694 *Continental Shelf Research* 20, 22. [https://doi.org/10.1016/S0278-4343\(00\)00065-0](https://doi.org/10.1016/S0278-4343(00)00065-0)
- 695 Ozdemir, C.E., 2016. Turbulence-resolving, two-phase flow simulations of wave-supported  
696 gravity flows: A conceptual study. *Journal of Geophysical Research: Oceans* 121, 8849–  
697 8871. <https://doi.org/10.1002/2016jc012061>
- 698 Patruno, S., Hampson, G.J., Jackson, C., 2015. Quantitative characterisation of deltaic and  
699 subaqueous clinoforms. *Earth-Science Reviews* 142, 79–119.
- 700 Patruno, S., Helland-Hansen, W., 2018. Clinoforms and clinoform systems: Review and  
701 dynamic classification scheme for shorelines, subaqueous deltas, shelf edges and  
702 continental margins. *Earth-Science Reviews* 185, 202–233.
- 703 Peng, Y., Olariu, C., Steel, R.J., 2020. Recognizing tide- and wave-dominated compound  
704 deltaic clinoforms in the rock record. *Geology* 48, 1149–1153.
- 705 Pirmez, C., Pratson, L.F., Steckler, M.S., 1998. Clinoform development by advection-  
706 diffusion of suspended sediment: Modeling and comparison to natural systems. *Journal*  
707 *of Geophysical Research: Solid Earth* 103, 24141–24157.  
708 <https://doi.org/10.1029/98JB01516>
- 709 Porter-Smith, R., Harris, P.T., Andersen, O.B., Coleman, R., Greenslade, D., Jenkins, C.J.,  
710 2004. Classification of the Australian continental shelf based on predicted sediment  
711 threshold exceedance from tidal currents and swell waves. *Marine Geology* 211, 1–20.  
712 <https://doi.org/10.1016/j.margeo.2004.05.031>
- 713 Puig, P., Ogston, A.S., Mullenbach, B., Nittrouer, C., Sternberg, R., 2003. Shelf-to-Canyon  
714 sediment-transport processes on the Eel Continental Margin (Northern California).

- 715 Marine Geology - MAR GEOLOGY 193, 129–149. <https://doi.org/10.1016/S0025->  
716 3227(02)00641-2
- 717 Ramirez, A.R., de Guzman, M.E., Dawson, T.E., Ackerly, D.D., 2020. Plant hydraulic traits  
718 reveal islands as refugia from worsening drought. *Conservation Physiology* 8.  
719 <https://doi.org/10.1093/conphys/coz115>
- 720 Ramsdell, R.C., Miedema, S.A., Talmon, A.M., Asme, O.O., Arctic Engn, D., 2011.  
721 HYDRAULIC TRANSPORT OF SAND/SHELL MIXTURES, in: 30th International  
722 Conference on Ocean, Offshore and Arctic Engineering. Rotterdam, NETHERLANDS,  
723 pp. 533-+.
- 724 Reid, J.L., Schwartzlose, R.A., 1962. Direct measurements of the Davidson Current off  
725 central California. *Journal of Geophysical Research* 67, 2491–2497.  
726 <https://doi.org/10.1029/jz067i006p02491>
- 727 Reimer, P.J., Austin, W.E.N., Bard, E., Bayliss, A., Blackwell, P.G., Ramsey, C.B., Butzin,  
728 M., Cheng, H., Edwards, R.L., Friedrich, M., Grootes, P.M., Guilderson, T.P., Hajdas,  
729 I., Heaton, T.J., Hogg, A.G., Hughen, K.A., Kromer, B., Manning, S.W., Muscheler, R.,  
730 Palmer, J.G., Pearson, C., Plicht, J. van der, Reimer, R.W., Richards, D.A., Scott, E.M.,  
731 Southon, J.R., Turney, C.S.M., Wacker, L., Adolphi, F., Büntgen, U., Capano, M.,  
732 Fahrni, S.M., Fogtmann-Schulz, A., Friedrich, R., Köhler, P., Kudsk, S., Miyake, F.,  
733 Olsen, J., Reinig, F., Sakamoto, M., Sookdeo, A., Talamo, S., 2020. The IntCal20  
734 Northern Hemisphere Radiocarbon Age Calibration Curve (0–55 cal kBP). *Radiocarbon*  
735 62, 725–757. <https://doi.org/10.1017/RDC.2020.41>
- 736 Reynolds, L.C., Simms, A.R., 2015. Late Quaternary relative sea level in Southern California  
737 and Monterey Bay. *Quaternary Science Reviews* 126, 57–66.  
738 <https://doi.org/10.1016/j.quascirev.2015.08.003>
- 739 Sanders, J.E., 1960. Primary Sedimentary Structures Formed by Turbidity Currents and  
740 Related Resedimentation Mechanisms.
- 741 Schattner, U., Lobo, F.J., Lopez-Quiros, A., Nascimento, JLD, de Mahiques, M.M., 2020.  
742 What feeds shelf-edge clinoforms over margins deprived of adjacent land sources? An  
743 example from southeastern Brazil. *Basin research* 32, 293-301.  
744 <https://doi.org/10.1111/bre.12397>
- 745 Scully, M.E., Friedrichs, C.T., Wright, L.D., 2003. Numerical modeling of gravity-driven  
746 sediment transport and deposition on an energetic continental shelf: Eel River, northern  
747 California. *Journal of Geophysical Research: Oceans* 108, 3120.  
748 <https://doi.org/10.1029/2002JC001467>
- 749 Sept, J.D., 2019. *The New Beachcomber's Guide to the Pacific Northwest*. Harbour  
750 Publishing.
- 751 Sequeiros, O.E., Naruse, H., Endo, N., Garcia, M.H., Parker, G., 2009. Experimental study on  
752 self-accelerating turbidity currents. *Journal of Geophysical Research* 114, C05025.  
753 <https://doi.org/10.1029/2008JC005149>
- 754 Snyder, G.R., Balster-Gee, A.F., Kluesner, J.W., Johnson, S.Y., Medri, E., Simms R., A.,  
755 Nishenko, S., Greene, G., Conrad, J.E., 2022. Geophysical and core sample data

756 collected offshore central California, during field activity 2019-651-FA.  
757 <https://doi.org/https://doi.org/10.5066/P9A0U8J7>

758 Sperazza, M., Moore, J.N., Hendrix, M.S., 2004. High-Resolution Particle Size Analysis of  
759 Naturally Occurring Very Fine-Grained Sediment Through Laser Diffractometry.  
760 *Journal of Sedimentary Research* 74, 736–743. <https://doi.org/10.1306/031104740736>

761 Stanford, J.D., Hemingway, R., Rohling, E.J., Challenor, P.G., Medina-Elizalde, M., Lester,  
762 A.J., 2011. Sea-level probability for the last deglaciation: A statistical analysis of far-  
763 field records. *Global and Planetary Change* 79, 193–203.  
764 <https://doi.org/10.1016/j.gloplacha.2010.11.002>

765 Steel, R., Olsen, T., 2002. Clinofolds, Clinofold Trajectories and Deepwater Sands, in:  
766 Sequence Stratigraphic Models for Exploration and Production: Evolving Methodology,  
767 Emerging Models, and Application Histories: 22nd Annual. SOCIETY OF ECONOMIC  
768 PALEONTOLOGISTS AND MINERALOGISTS, pp. 367–380.  
769 <https://doi.org/10.5724/gcs.02.22.0367>

770 Storlazzi, C.D., Griggs, G.B., 2000. Influence of El Niño-Southern Oscillation (ENSO)  
771 events on the evolution of central California's shoreline. *Geological Society of America*  
772 *Bulletin* 112, 236–249. [https://doi.org/10.1130/0016-](https://doi.org/10.1130/0016-7606(2000)112<236:IOENOE>2.0.CO;2)  
773 [7606\(2000\)112<236:IOENOE>2.0.CO;2](https://doi.org/10.1130/0016-7606(2000)112<236:IOENOE>2.0.CO;2)

774 Storlazzi, C.D., Wingfield, D.K., 2005. Spatial and Temporal Variations in Oceanographic  
775 and Meteorologic Forcing Along the Central California Coast, 1980-2002. U.S.  
776 Geological Survey.

777 Stuiver, M., Reimer, P.J., Reimer, R.W., 2022. CALIB 14C Calibration Program.

778 Traykovski, P., Wiberg, P.L., Geyer, W.R., 2007. Observations and modeling of wave-  
779 supported sediment gravity flows on the Po prodelta and comparison to prior  
780 observations from the Eel shelf. *Continental Shelf Research* 27, 375–399.  
781 <https://doi.org/10.1016/j.csr.2005.07.008>

782 Vericat, D., Batalla, R.J., Garcia, C., 2006. Breakup and reestablishment of the armour layer  
783 in a large gravel-bed river below dams: The lower Ebro. *Geomorphology* 76, 122–136.  
784 <https://doi.org/10.1016/j.geomorph.2005.10.005>

785 Wright, L.D., Friedrichs, C.T., 2006. Gravity-driven sediment transport on continental  
786 shelves: A status report. *Continental Shelf Research* 26, 2092–2107.  
787 <https://doi.org/10.1016/J.CSR.2006.07.008>

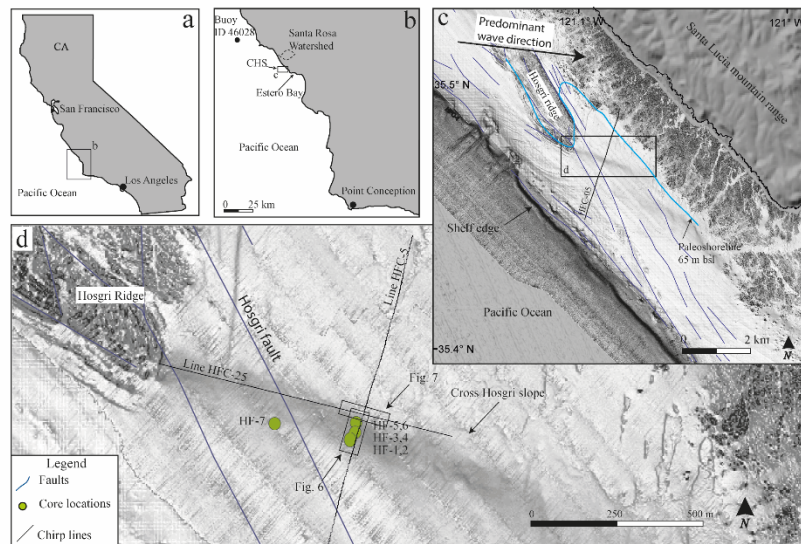
788 Wright, L.D., Friedrichs, C.T., Kim, S.C., Scully, M.E., 2001. Effects of ambient currents and  
789 waves on gravity-driven sediment transport on continental shelves. *Marine Geology* 175,  
790 25–45. [https://doi.org/10.1016/S0025-3227\(01\)00140-2](https://doi.org/10.1016/S0025-3227(01)00140-2)

791 Yousefi, M., Milne, G.A., Love, R., Tarasov, L., 2018. Glacial isostatic adjustment along the  
792 Pacific coast of central North America. *Quaternary Science Reviews* 193, 288–311.  
793 <https://doi.org/10.1016/j.quascirev.2018.06.017>

794 Yue, L., Cheng, Z., Hsu, T., 2020. A Turbulence-Resolving Numerical Investigation of  
795 Wave-Supported Gravity Flows. *Journal of Geophysical Research: Oceans* 125.  
796 <https://doi.org/10.1029/2019JC015220>

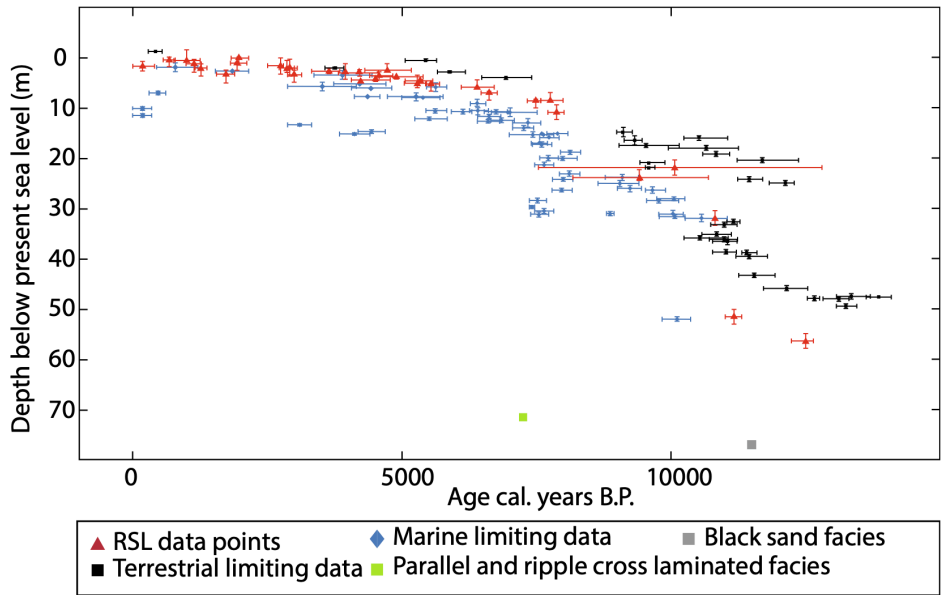
797 Zecchin, M., Catuneanu, O., Caffau, M., 2019. Wave-ravinement surfaces: Classification and  
798 key characteristics. *Earth-Science Reviews* 188, 210–239.  
799 <https://doi.org/10.1016/j.earscirev.2018.11.011>

800



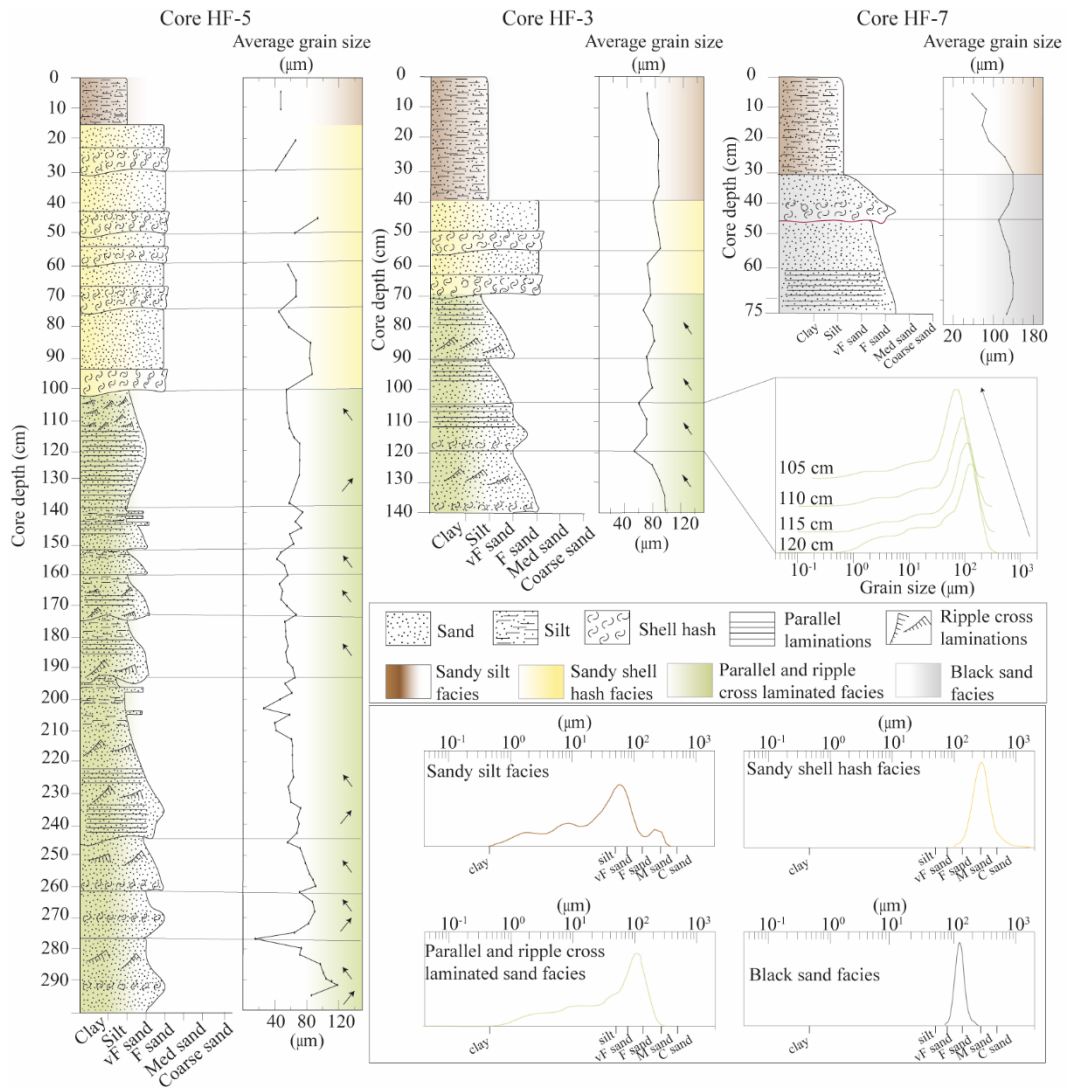
801

802 **Figure 1:** (a) Map of California highlighting the study area. (b) Location in California of the  
803 study area. (c) Shaded relief of the continental shelf in the study area based on multibeam  
804 bathymetry (California State University Monterey Bay Sea Floor Mapping Lab [CSUMB],  
805 2012; Hartwell et al., 2013). (d) Shaded relief of the study area, highlighting the location of  
806 cores, previously mapped faults (blue lines), and the chirp profile.



807

808 **Figure 2:** The age and elevation of radiocarbon ages obtained from the parallel and ripple  
 809 cross laminated facies (green square) and the black sand facies (gray square) plotted  
 810 alongside the relative sea-level constraints for southern California compiled by Reynolds and  
 811 Simms (2015, Fig. 2).

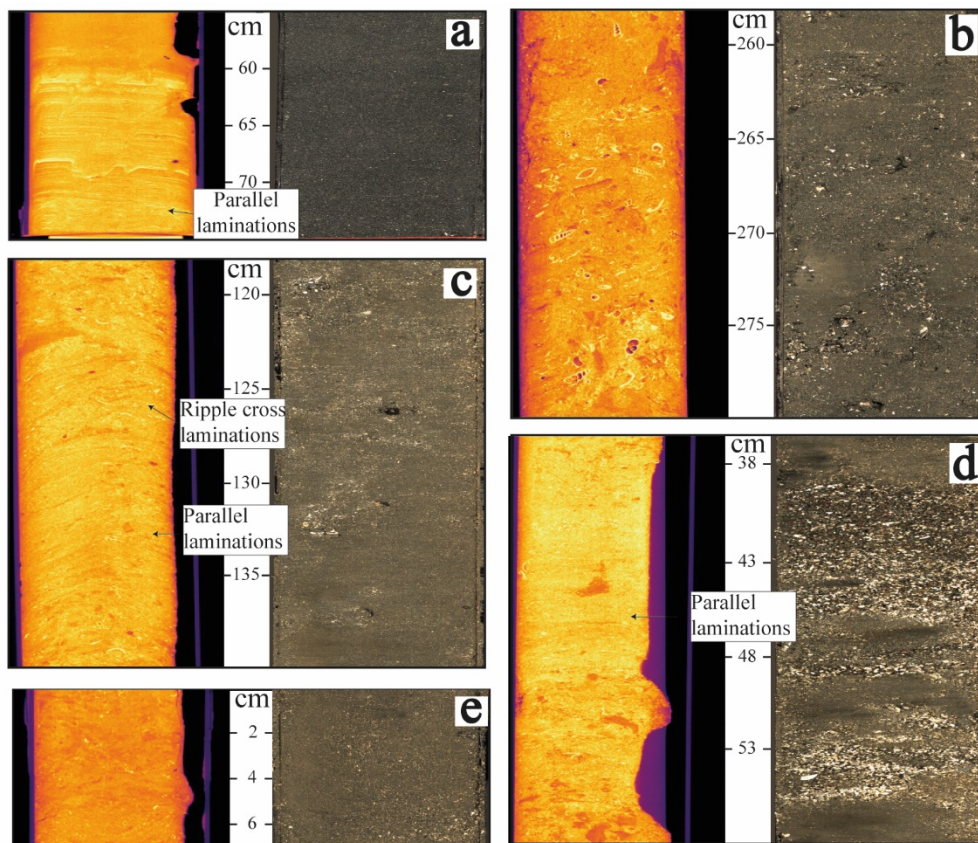


812

813 **Figure 3:** Stratigraphic profiles, average grain size, and representative facies grain size

814 distributions (bottom panel) for cores HF-3, HF-5, and HF-7.

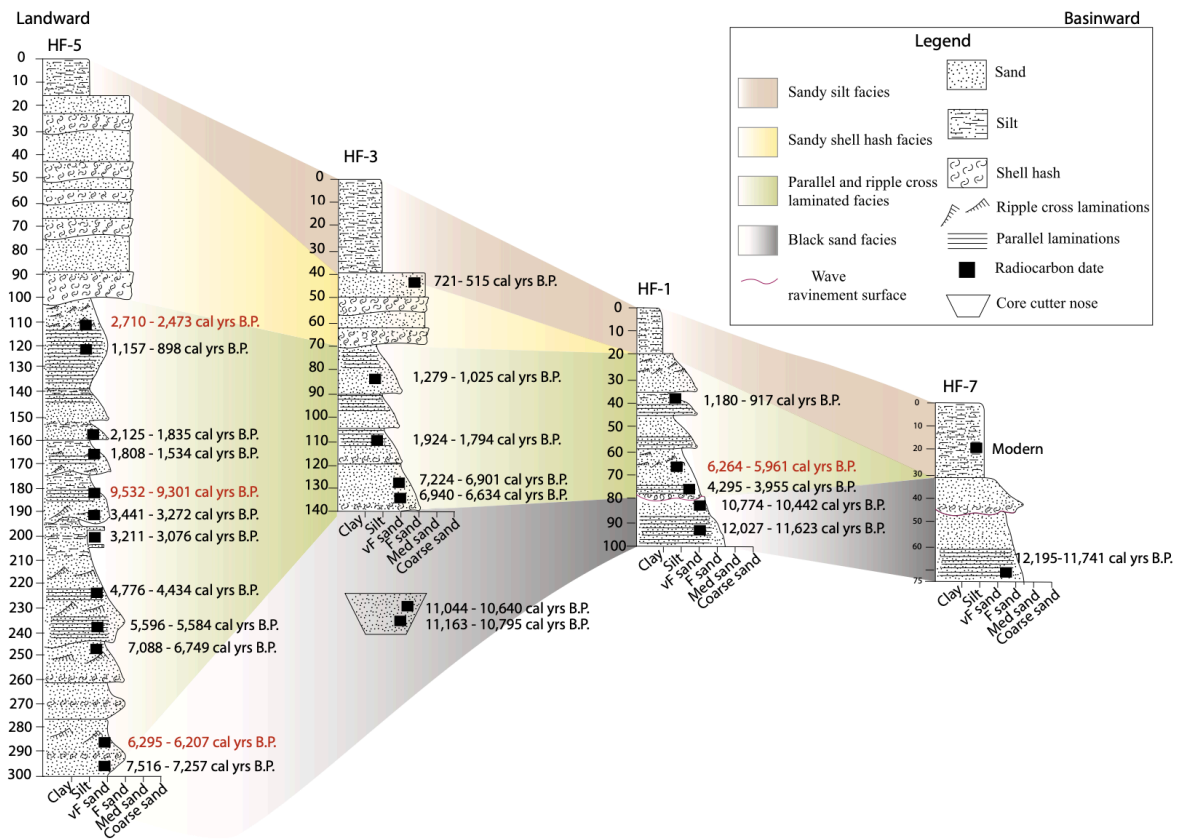




815

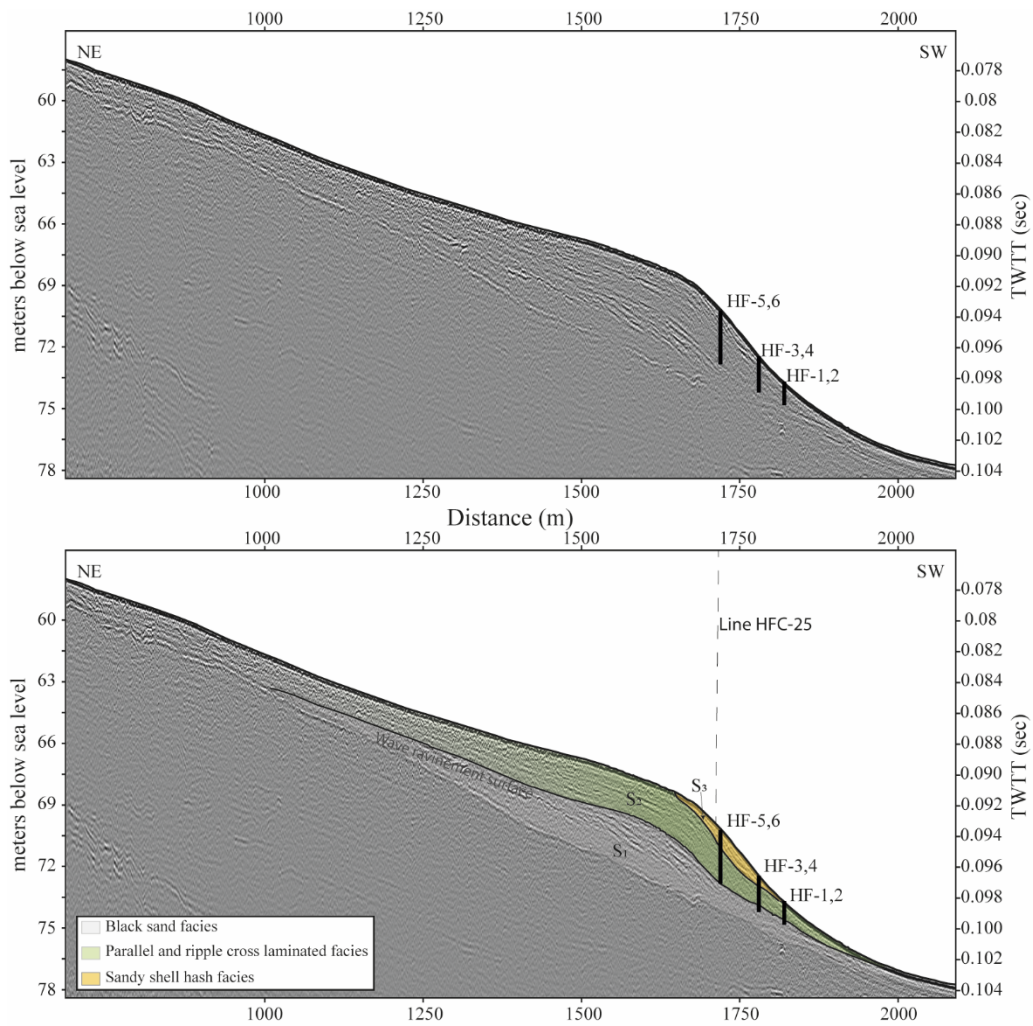
816 **Figure 4:** Photographs (right) and Computed Tomography (CT) scans (left) of the  
 817 sedimentary facies identified in the cores. a) Black sand facies. Photograph and CT scan from  
 818 core HF-7 at depth 75-55 cm. b) Parallel and ripple cross laminated facies, showing the  
 819 coarsening upward portion. Photograph and CT scan from core HF-5 at depth 280-258 cm. c)  
 820 Parallel and ripple cross laminated facies, showing the fining upward portion. Photograph and  
 821 CT scan from core HF-5 at depth 140-118 cm. d) Sandy shell hash facies. Photograph and CT  
 822 scan from core HF-5 at depth 58-36 cm. e) Sandy silt facies. Photograph and CT scan from  
 823 core HF-7 at depth 7-0 cm.

824



825

826 **Figure 5:** Stratigraphic logs and correlations from four cores collected on the Cross Hosgri  
 827 Slope (CHS), along with radiocarbon ages. Dates marked in red are interpreted as out of  
 828 sequence ages and highlighted by \* in Table 2.



829

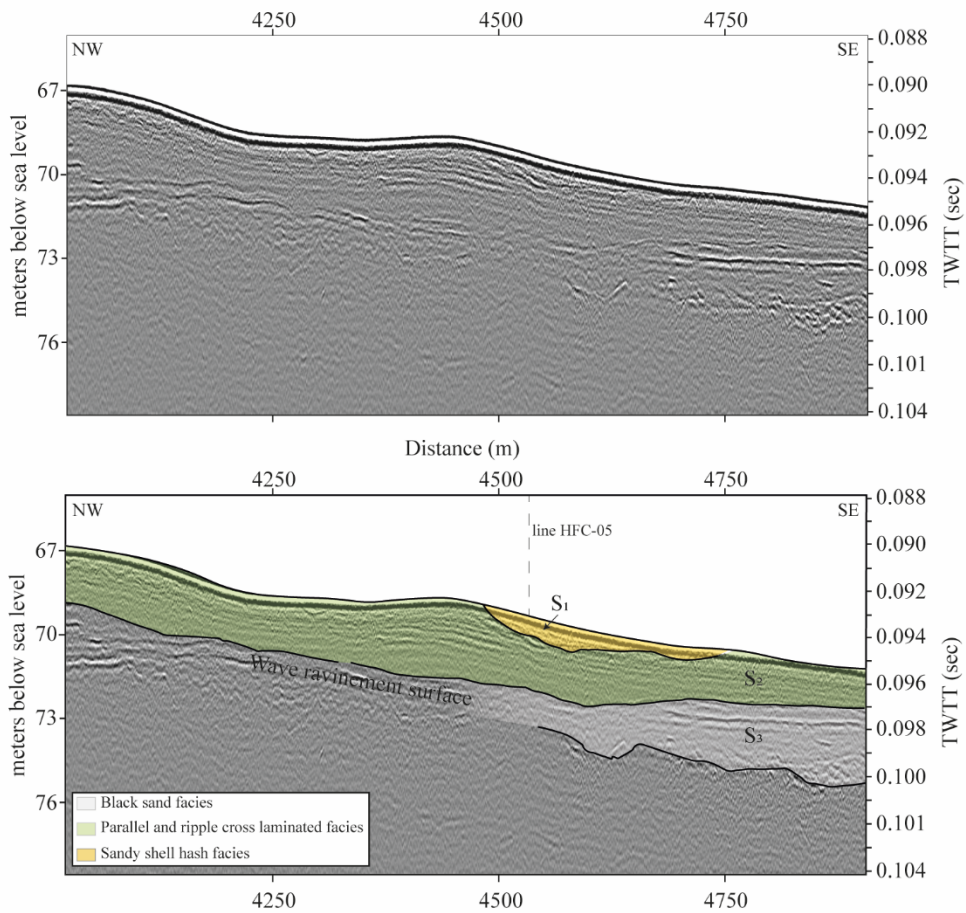
830 **Figure 6:** Seismic line HFC-5 across the Cross Hosgri Slope (CHS; see Fig. 1 for location).

831 Upper profile is shown without interpretations. Lower profile shows seismic units  $S_1$  (gray),

832 coinciding with the black sand facies,  $S_2$  (green) comprised of the parallel and ripple cross

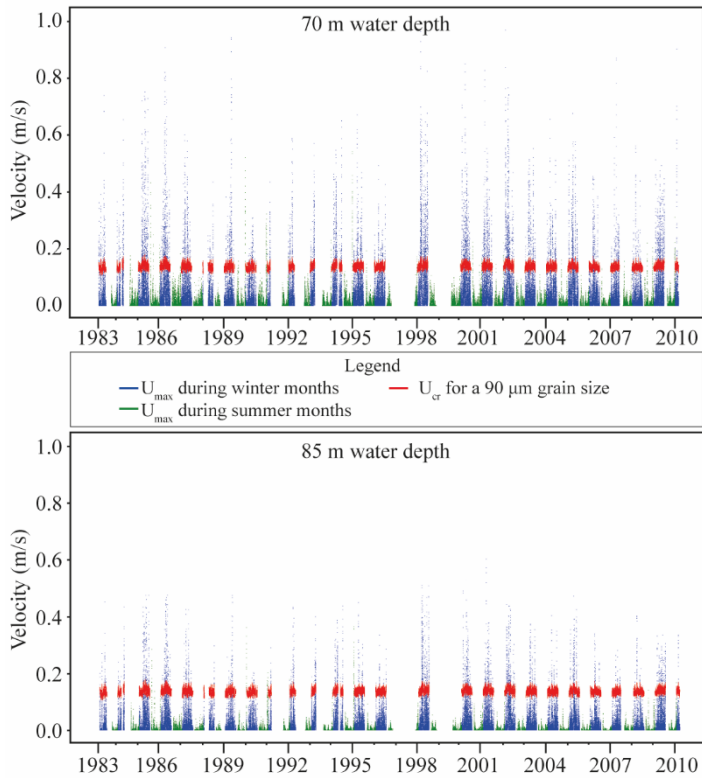
833 laminated facies and the sandy silt facies, and  $S_3$  (yellow) comprised of the uppermost

834 portion of the sandy shell hash facies and the silty sand facies. VE ~ 32.



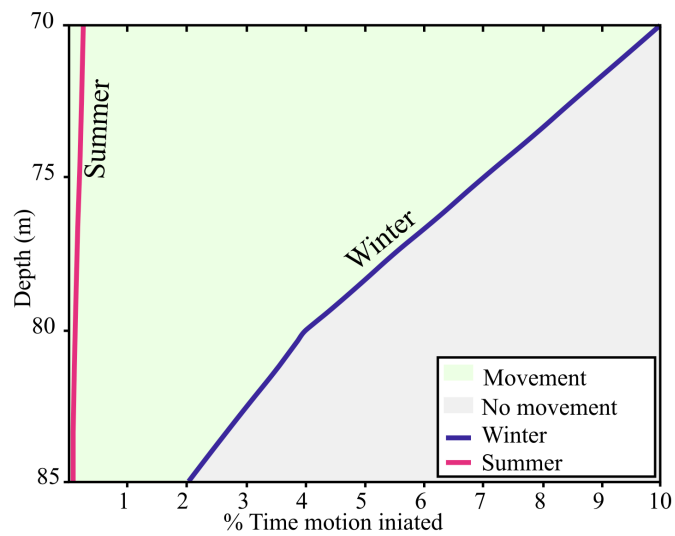
835

836 **Figure 7:** Seismic line HFC-25 along strike of the Cross Hosgri Slope (CHS; see Fig. 1 for  
 837 location). Upper profile is shown without interpretations. Lower profile shows seismic units  
 838 S<sub>1</sub> (gray), coinciding with the black sand facies, S<sub>2</sub> (green) comprised of the parallel and  
 839 ripple cross laminated facies and the sandy silt facies, and S<sub>3</sub> (yellow) comprised of the  
 840 uppermost portion of the sandy shell hash facies and the silty sand facies. VE ~34.



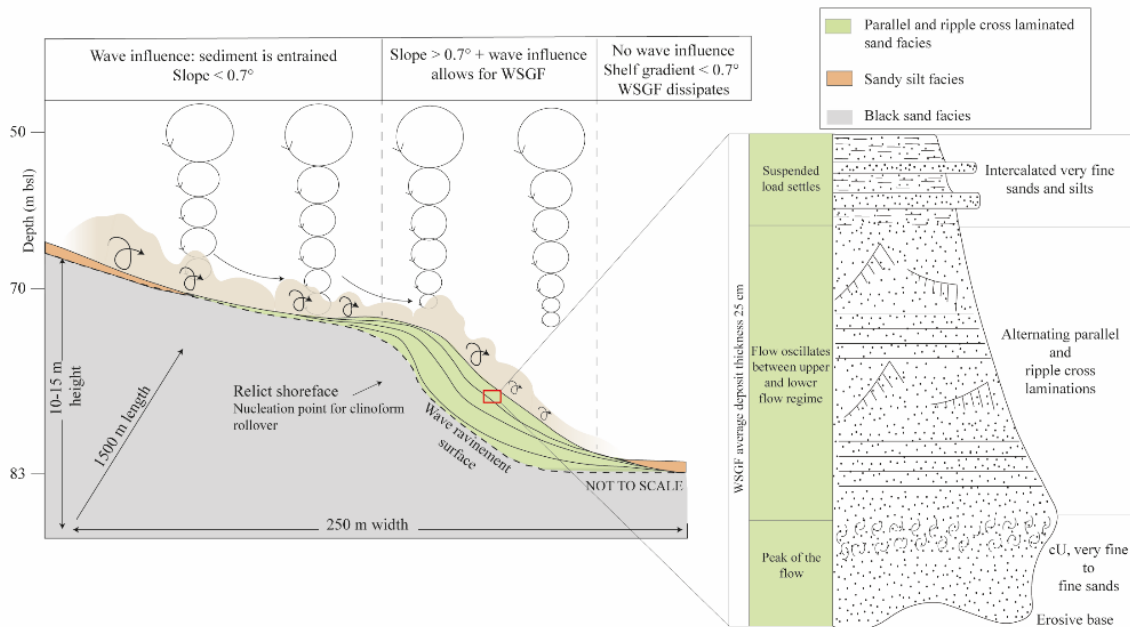
841

842 **Figure 8:** Values of  $U_{max}$  and  $U_{cr}$  calculated from wave data northwest of Estero Point  
 843 (NOAA.gov, station ID: 46028) from 1983 to 2010. Top panel shows  $U_{max}$  and  $U_{cr}$  at 70 m  
 844 water depth during winter (October-March) and summer (April-September) months. Bottom  
 845 panel shows  $U_{max}$  and  $U_{cr}$  at 85 m water depth during winter (October-March) and summer  
 846 (April-September) months.



847

848 **Figure 9:** Plot showing % time during which  $U_{max} > U_{cr}$  for a grain size of 90  $\mu\text{m}$  and how  
 849 this condition varies with increasing depth, both in summer conditions and winter conditions.  
 850



851  
 852 **Figure 10:** Diagram depicting mode of sediment transport and deposition along the Cross  
 853 Hpsgri Slope (CHS) subaqueous clinoform in a sandy environment with no direct riverine  
 854 input (left). Facies model for the wave-supported gravity flows (WSGF) deposit along the  
 855 foreset of the subaqueous clinoform (right).

856

Core #	Length (m)	Depth (m)	Latitude	Longitude
HF-1	0-97	82	35 28.5902	121 04.4682
HF-2	0-109	80	35 28.5902	121 04.4682
HF-3	0-143	73	35 28.6101	121 04.4610
HF-4	0-172	73.5	35 28.6101	121 04.4610
HF-5	0-297	71.6	35 28.6407	121 04.4502
HF-6	0-260	72	35 28.6407	121 04.4502

HF-7	0-77	81	35 28.6440	121 04.8010
------	------	----	------------	-------------

857

858 <sup>1</sup> Core lengths, water depths, and locations.

859

UCIAMS #	Core	Depth (cm)	Material/species	D <sup>14</sup> C ‰	±	<sup>14</sup> C age	±	Calibrated age (Cal years B.P.)
254929	HF-1	46	<i>Amphissa versicolor</i>	-186.7	1.3	1660	15	1180-917
254931	HF-1	61	<i>Neverita lewisi</i>	-519.68	1.0	5890	20	<b>6264-5961*</b>
254930	HF-1	80	<i>Amphissa versicolor</i>	-408.7	1.3	4220	20	4295-3955
254932	HF-1	90	<i>Clathurella canfieldi</i>	-705.8	0.6	9825	20	10774-10442
254936	HF-1	97	<i>Truncatella californica</i>	-734.9	0.6	10665	20	12027-11623
260440	HF-2	103.5	Gastropod	-730.1	0.7	10520	25	11808-11386
260441	HF-2	106	Gastropod	-712.3	0.7	10010	20	11085-10714
246214	HF-3	Cutter nose	<i>Callianax baetica</i>	-710.30	0.7	9950	20	11044-10640
230405	HF-3	VC cutter nose	<i>Gastropod</i>	-714.6	0.9	10075	25	11163-10795
243289	HF-3	137	<i>Amphissa versicolor</i>	-555.3	0.8	6510	15	6940-6634
230406	HF-3	131	<i>Gastropod</i>	-568.3	1.1	6750	25	7224-6901
243298	HF-3	110	Wood	-213.6	1.2	1930	15	1924-1794
243290	HF-3	80	Bivalve	-196.2	1.4	1755	15	1279-1025
243291	HF-3	40	<i>Amphissa versicolor</i>	-140.9	1.5	1220	15	721-515
260442	HF-4	154	<i>Turritella cooperi</i>	-683.2	0.7	9235	20	10035-9620
260443	HF-4	171.5	Gastropod	-679.2	0.7	9135	20	9857-9524

243299	HF-5	115	Wood	-265.7	1.2	2480	15	<b>2710-2473*</b>
243292	HF-5	122	<i>Amphissa versicolor</i>	-183.2	1.3	1625	15	1157-898
254938	HF-5	155	<i>Amphissa versicolor</i>	-267.4	1.2	2500	15	2125-1835
254933	HF-5	166	<i>Amphissa versicolor</i>	-243.7	1.2	2245	15	1808-1534
254935	HF-5	175	<i>Callianax baetica</i>	-670.7	0.6	8920	20	<b>9532-9301*</b>
254945	HF-5	180	Wood	-323.6	1.1	3140	15	3441-3272
254944	HF-5	199	Wood	-309.4	1.1	2975	15	3211-3076
254937	HF-5	222	<i>Amphissa versicolor</i>	-434.4	0.9	4575	15	4776-4434
246230	HF-5	233	Wood	-451.8	0.9	4830	15	5594-5484
243293	HF-5	255	<i>Callianax baetica</i>	-561.5	0.7	6625	15	7088-6749
243300	HF-5	287	Wood	-492.6	0.9	5450	15	<b>6295-6207*</b>
260444	HF-5	296	<i>Turritella cooperi</i>	-586.1	0.9	7085	20	<b>7516-7257</b>
254934	HF-7	20	<i>Amphissa versicolor</i>	8.2	1.6	Modern		
246207	HF-7	70	<i>Callianax baetica</i>	-737.6	0.7	10750	25	12195-11741

860

861 <sup>2</sup> Radiocarbon ages obtained during this study. Ages in bold and marked by an asterisk

862 indicate the ages interpreted as out of sequence.

863

Facies	Sedimentary structures	Other features	Mean grain size	Deposition mode/Interpreted environment	Occurrence (yrs B.P.)
Black Sand	-Well developed parallel laminations	-Shell fragments <5% -Well sorted, clean sand	130 µm	-Inner shelf -Shoreface	~ 12 – 10 ka



	-cU then fU			-WSGF	
Parallel and ripple	sequences	-Shell fragments	90 μm	-Distal	~ 7 ka- 900 ybp
cross laminated	-Ripple cross	20-25%		-Mid shelf slope	
facies	laminations				
	-Parallel				
	laminations				
Sandy shell hash			330 μm	-Storm wave	
	-Faint parallel	-Shell fragments		resuspension	~ 7 ka- 900 ybp
	laminations	~35%, up to 5 cm		-Proximal	
		in size		-Mid shelf slope	
Sandy silt	-Massive	-Shell fragments	40 μm	-Suspension settling	< 700 ybp
		3-5%		-Mid shelf	

864 <sup>3</sup> Description and interpretation of the depositional regimes and environments of the four

865 facies identified in the cores and their approximate age.

866

867